


# Bisphenol S Exposure and MASLD: A Mechanistic Study in Mice

Shiqi Li,<sup>1,2,3\*</sup> Yun Fan,<sup>2,3\*</sup> Min Tang,<sup>2,3\*</sup> Xiaorong Wu,<sup>4</sup> Shengjun Bai,<sup>2,3</sup> Xiancheng Yang,<sup>2,3</sup> Xueer Zhang,<sup>2,3</sup> Chuncheng Lu,<sup>3</sup> Chenbo Ji,<sup>1</sup> Paul A. Wade,<sup>5</sup> Xu Wang,<sup>1</sup> Wei Gu,<sup>1</sup> Guizhen Du,<sup>2,3</sup> and Yufeng Qin<sup>1,2,3</sup> 

<sup>1</sup>Department of Endocrinology, Genetics and Metabolism, Children's Hospital of Nanjing Medical University, Nanjing, China

<sup>2</sup>Department of Microbiology and Infection, School of Public Health, Nanjing Medical University, Nanjing, China

<sup>3</sup>Key Laboratory of Modern Toxicology of Ministry of Education, School of Public Health, Nanjing Medical University, Nanjing, China

<sup>4</sup>School of Public Health, Southwest Medical University, Luzhou, China

<sup>5</sup>Eukaryotic Transcriptional Regulation Group, Epigenetics and Stem Cell Biology Laboratory, National Institute of Environmental Health Sciences, Research Triangle Park, North Carolina, USA

**BACKGROUND:** Bisphenol S (BPS) is a substitute for bisphenol A in various commercial products and is increasingly used globally due to restrictions on bisphenol A usage. Consequently, there are increasing public health concerns that substantial effects mediated by synthetic chemicals may impact human health. Recently, epidemiology studies reported associations between bisphenol exposure and nonalcoholic fatty liver disease [metabolic dysfunction-associated steatotic liver disease (MASLD)]. However, the causal relationship and the molecular mechanisms affecting hepatocellular functions are still unknown.

**OBJECTIVES:** Our study aimed to understand the molecular mechanism by which BPS exposure caused hepatic lipid deposition.

**METHODS:** C57BL/6J mice were exposed to BPS for 3 months, and its effects were assessed by histology. RNA sequencing (RNA-seq), assay for transposase-accessible chromatin with high-throughput sequencing (ATAC-seq), and cleavage under targets and tagmentation (CUT&Tag) were used to investigate mechanistic details. ATF3 liver-specific knockout mice and cells were used to validate its functions in BPS-induced hepatotoxicity.

**RESULTS:** Here, mice that were chronically exposed to BPS showed significant lipid deposition in the liver and dyslipidemia and were predisposed to MASLD, accompanied with a reprogrammed liver transcriptional network and chromatin accessibility that was enriched for the Atf3 binding motif. Comparing to the control group, we identified numerous differential Atf3 binding sites associated with signaling pathways integral to lipid catabolism and synthesis in the BPS exposure group, resulting in a drastic surge in lipid accumulation. Moreover, knocking out Atf3 *in vitro* and *in vivo* significantly attenuates BPS-induced hepatic lipid accumulation via the regulation of chromatin accessibility and gene expression. Besides, inhibiting JunB also eliminates BPS-induced Atf3 upregulation and lipid accumulation.

**CONCLUSION:** Our study reveals a novel mechanism, through which BPS upregulates JunB and Atf3 to impair hepatic lipid metabolism, and provides new insights into the hepatotoxicity of BPS. <https://doi.org/10.1289/EHP17057>

## Introduction

Metabolic dysfunction-associated steatotic liver disease (MASLD) is a leading cause of chronic liver disease that affects an estimated 1 billion individuals worldwide and is expected to continue to rise dramatically.<sup>1,2</sup> MASLD is characterized by fat-filled liver cells and comprises a spectrum of histopathologic abnormalities without excessive alcohol use.<sup>3,4</sup> It is closely associated with metabolic disorders, while environmental exposure can also damage the hepatic metabolism resulting in the development of MASLD.<sup>5</sup> Numerous epidemiological studies revealed that environmental exposure to bisphenols was associated with disrupted lipid metabolism and MASLD in humans.<sup>6,7</sup> Animal studies also demonstrated that bisphenol exposure resulted in the destruction of liver

structure, dyslipidemia, inflammation, and the progression of MASLD.<sup>8,9</sup>

Among all of the bisphenol analogues, bisphenol S (BPS) is now highly manufactured and applied in the production of food cans and plastic bottles, since bisphenol A has been restricted in many countries and gradually withdrawn from the market.<sup>10</sup> This inevitably led to BPS contamination of the environment and subsequent human exposure. BPS can now be detected in indoor dust and even in human urine and serum.<sup>11,12</sup> Multiple epidemiological studies reported that BPS exposure was associated with metabolic diseases, reproductive diseases, and cancer.<sup>10,13–16</sup> However, the molecular mechanisms responsible for BPS-induced hepatotoxicity and its contribution to MASLD remain to be elucidated.

The liver serves as the major detoxification organ of the body, involved in metabolizing exogenous chemicals.<sup>17</sup> It is also responsible for the uptake, synthesis, and secretion of lipids.<sup>18</sup> Our previous studies revealed that liver chromatin dynamics mediated hepatic gene regulation and adaptation to excessive lipid accumulation in mice.<sup>19</sup> Hepatocellular regulation of gene expression in response to environmental cues is largely reliant on transcription factors, which prefer to bind to DNA at accessible chromatin regions.<sup>20–23</sup> Animal studies reported that exposure to bisphenols resulted in changes in chromatin accessibility and histone modifications.<sup>24–27</sup> However, few studies have focused on the chromatin accessibility and gene regulations during BPS exposure and progression to dyslipidemia leading to MASLD.

Here, using assay for transposase-accessible chromatin with high-throughput sequencing (ATAC-seq), cleavage under targets and tagmentation (CUT&Tag), and RNA sequencing (RNA-seq), we aimed to identify alteration of chromatin accessibility and gene regulation between lipid synthesis and catabolism in response to BPS exposure in hepatic cells and liver tissues. Our findings may provide new insight into the mechanistic implications of hepatic toxicity induced by BPS and how hepatic chromatin organization contributes to MASLD during environmental stimulation.

\*The first three authors contributed equally to this study, and they should be regarded as joint first authors.

Address correspondence to Yufeng Qin. Telephone: +86-25-86868426. Email: [qiny@njmu.edu.cn](mailto:qiny@njmu.edu.cn). And, Guizhen Du. Email: [guizhendu@njmu.edu.cn](mailto:guizhendu@njmu.edu.cn). And, Wei Gu. Email: [guwei154@njmu.edu.cn](mailto:guwei154@njmu.edu.cn)

Supplemental Material is available online (<https://doi.org/10.1289/EHP17057>).

The authors declare no conflict of interest.

Conclusions and opinions are those of the individual authors and do not necessarily reflect the policies or views of EHP Publishing or the National Institute of Environmental Health Sciences.

*EHP* is a Diamond Open Access journal published with support from the NIEHS, NIH. All content is public domain unless otherwise noted. Contact the corresponding author for permission before any reuse of content. [Full licensing information](#) is available online.

Received 24 December 2024; Revised 22 March 2025; Accepted 3 April 2025; Published 14 May 2025.

**Note to readers with disabilities:** *EHP* strives to ensure that all journal content is accessible to all readers. However, some figures and Supplemental Material published in *EHP* articles may not conform to 508 standards due to the complexity of the information being presented. If you need assistance accessing journal content, please contact [ehpsubmissions@niehs.nih.gov](mailto:ehpsubmissions@niehs.nih.gov). Our staff will work with you to assess and meet your accessibility needs within 3 working days.

## Materials and Methods

### Animals and Treatments

All mouse experiments were performed in accordance with the procedure approved by the Institutional Animal Care and Use Committee (IACUC) (IACUC-2012025) at Nanjing Medical University. Twenty-four 7-week-old C57BL/6 male mice were obtained from the experiment animal center of Nanjing Medical University and acclimated for 1 week before the study. During the study, four mice were housed in each cage. According to an US EPA report in 2015, they proposed the no-observed-adverse-effect level (NOAEL) of BPS was 10 mg/kg/day for systemic effects.<sup>28</sup> The European Food Safety Authority (EFSA) designated the NOAEL of BPS to be 60 mg/kg BW/day for general systemic toxicity, 20 mg/kg BW per day for developmental toxicity, and 180 mg/kg BW/day for reproductive toxicity in the 2020 EFSA report.<sup>29</sup> We used 0.1 mg/kg BW/day (BPS-L) and 1 mg/kg BW/day (BPS-H) as exposure dosages in the animal study, which are 10–200 times lower than the NOAELs of BPS (10–180 mg/kg BW). A pregnancy cohort study detected serum BPS concentrations ranging from nondetectable (ND) to 140 ng/mL.<sup>30</sup> Chronic BPS exposure at 5 mg/kg BW/day in mice yielded serum concentrations of 5.47–11.78 ng/mL,<sup>31</sup> effectively modeling human-relevant exposure levels observed in epidemiological study.<sup>30</sup> In this study, serum BPS concentrations in the BPS-H group ranged from 0.7 to 5.85 ng/mL (Excel Table S1). The BPS (purity ≥99%; Aladdin) was purchased and dissolved in 0.1% dimethylsulfoxide (DMSO) to make stock solution (100 mg/mL for BPS-L and 1,000 mg/mL for BPS-H) and stored at –4°C. The stock solutions were prepared once a week, and working solutions were prepared every 2 d. Mice were exposed to BPS by oral gavage every day for 12 wk.

Atf3<sup>fx/fx</sup> mice were generated using the CRISPR/Cas9 gene-editing system by Cyagen Biosciences Inc. (S-CKO-01328, CKOCMP-11910-Atf3-B6N-VA; Cyagen). Exon 3 and 4 were selected as conditional knockout regions. The primers for genotyping are as follows: forward primer: 5'-ACACCAACTGTTTGGCACTAAGA-3', reverse primer: 5'-GTATGCTCAGAGAACTGATGGC-3'. Liver Atf3 knockout mice were constructed by crossing Atf3<sup>fx/fx</sup> mice with Alb-Cre mice (Cyagen). The primers for LKO genotyping are as follows: forward primer: 5'-ACTCCAGAGGGAAGGACAACCTT-3', reverse primer: 5'-GTATGCTCAGAGAACTGATGGC-3'. PCR was performed using 2 × Rapid Taq Master Mix (Vazyme) on Bio-Rad T100 PCR (Bio-Rad) with the following conditions: 95°C for 5 min, followed by 35 cycles of denaturation at 94°C for 30 s, annealing at 62°C for 35 s, and extension at 72°C for 35 s. Eighteen 8-week-old male mice were used, and four to five mice were housed in each cage during the study. The BPS (purity ≥99%; Aladdin) was dissolved in 0.1% DMSO to make stock solution (1,000 mg/mL) and stored at –4°C. The stock solution was prepared once a week, and working solution was prepared every 2 d. Mice were exposed to BPS by oral gavage every day for 12 wk.

All animals were maintained in Specific Pathogen Free (SPF)-level environments with a temperature of 19–23°C, a 12-h light and dark cycle, and free access to water and diet during the entire study. The mice were euthanized by CO<sub>2</sub> on the last day of treatment. The body weight of each mouse was recorded weekly. Blood was collected from the medial canthus vein and incubated at room temperature for 1 h to allow coagulation. After centrifuging at 1,000 × g/min for 10 min at 4°C, the serum was collected and stored immediately at –80°C. Liver tissue was harvested and weighed, one half of each liver was fixed with 4% formaldehyde for 24 h, and the remaining half from the same mouse was frozen with liquid nitrogen and stored at –80°C until further analysis.

### Histological Analysis

For hematoxylin and eosin (H&E) and Sirius Red staining, liver tissues were collected and fixed as described above. Fixed liver tissues were embedded in paraffin and cut into 5-μm sections (Thermo; HM340E). Paraffin sections were prepared and stained with hematoxylin and eosin (three samples/group) or Sirius Red (three samples/group). For Oil Red O staining (three samples/group), liver tissues were frozen and embedded in optimum cutting temperature compound (OCT), which were sectioned into 8-μm slices and stained with Oil Red O. Staining images were obtained and analyzed using a light microscope (3DHISTECH KFT, Panoramic SCAN, EU).

### Cell Lines

The AML12 cells were obtained from YUCHI Biotechnology (YUCHI) and cultured in Dulbecco's modified Eagle medium (DMEM)/F12 containing 10% fetal bovine serum (FBS), 40 ng/mL dexamethasone, 5.5 μg/mL transferrin, 5 ng/mL selenium, 10 μg/mL insulin, and 1% antibiotics (YUCHI). CRISPR-Cas9 was used to construct the Atf3 knockout cell line. The target sequence of gRNA used was 5'-tgactctgaggcagag-3' and ordered from Tsingke. Briefly, oligos were annealed in T4 DNA ligase buffer (SD0267; TaKaRa) and phosphorylated using T4 PNK (2021A; TaKaRa). The annealed oligos and *BbsI* (ER1012; Thermo Fisher)-linearized PX459 plasmid (62988; Addgene) were ligated using T4 DNA ligase (2011A; TaKaRa) at room temperature. The vectors were sent to Novogene for verification by Sanger sequencing. The 293T cells were cultured in DMEM containing 10% fetal bovine serum at 37°C under 5% CO<sub>2</sub>. Upon reaching 70–80% confluence, cells were passaged and seeded at a density of 1 × 10<sup>5</sup> cells. One day after seeding, lentivirus was prepared by transfecting 293T cells with 2.5 μg pX459, 1.5 μg pPAX2 (12260; Addgene), and 1 μg pMD2.G (12259; Addgene) plasmids using Lipo3000 (L3000015; Thermo Fisher). Virus-containing medium was harvested by centrifuging the supernatant culture medium at 20,000 Relative Centrifugal Force (RCF) for 10 min 2 d after transfection. About 6 × 10<sup>5</sup> AML12 cells were seeded on six-well plates the day before infection. Cells were infected with 2 mL virus-containing medium and polybrene (at a final concentration of 8 μg/mL) for 8 h. After changing the medium, infected cells were cultured for 24 h and selected with puromycin (at a final concentration of 1 μg/mL) for 2 d. Then, 1,000 cells were transferred to a 10-cm plate. After 10–12 d, the single cell-derived clones were picked into 96-well plates and allowed to grow for another 2–3 d to verify ATF3 knockout efficiency by western blot (WB). The details are described in the Western Blot section of the Methods. Correctly targeted cells were cultured for cryopreservation or other experiments. The 293T cells and all plasmids used in the study were kindly provided by Professor Pishun Li.

### Primary Mouse Hepatocytes Isolation

Primary mouse hepatocytes were isolated by standard two-step perfusion from collagenase perfusion technique.<sup>32</sup> Briefly, 8-week-old C57BL/6 male mice received 50 mg/kg pentobarbital sodium (Sigma-Aldrich; P3761) and underwent laparotomy. The portal vein was cannulated and then perfused with 25 mL perfusion medium [D-HANKS containing 0.5 mM Ethylene Glycol Tetraacetic Acid (EGTA), 25 mM 4-(2-Hydroxyethyl)piperazine-1-ethanesulfonic acid (HEPES), and 1% Penicillin-Streptomycin (P/S)] followed by 25 mL digest medium (DMEM containing 100 CDU/mL Collagenase IV, 3 mM CaCl<sub>2</sub>, 15 mM HEPES, and 1% P/S). The liver was removed and then hepatocytes were mechanically dissociated and released in dispersion buffer (DMEM containing 100 nM dexamethasone, 0.5 μg/mL bovine insulin, 15 mM

HEPES, 1% P/S, and 10% FBS), filtered through a 70  $\mu$ M filter and purified with a density gradient centrifugation. The cells were cultured in dispersion buffer for the first 4 h, and then the medium was changed into culture medium (DMEM containing 100 nM dexamethasone, 0.5  $\mu$ g/mL bovine insulin, 5 mM HEPES, and 1% antibiotics).

### Cell Viability Assay

Cell viability was assessed to determine the BPS dosage in the cell experiment. Briefly, cells were seeded in 96-well plates at a density of  $\sim$ 5K cells per well and treated with BPS for 24 h from 0.1 to 100  $\mu$ M according to its benchmark dose lower confidence limit (BMDL) (82.2  $\mu$ M).<sup>33</sup> After removing the culture medium, 100  $\mu$ L solution, including 10  $\mu$ L CCK-8 (BS350B; Biosharp) and 90  $\mu$ L medium, was added to the plates and incubated for another 1 h at 37°C under 5% CO<sub>2</sub>. After incubation, the absorbance was determined at 450 nm (TECAN Infinite M200 PRO).

### Nile Red Staining

Cells were seeded at  $2 \times 10^5$  cells per well in a six-well plate (Cellvis). After 24 h BPS or AP-1 inhibitor (SR11302; 2  $\mu$ M) (MedChemExpress; HY-15870) treatment, cells were washed twice by phosphate-buffered saline (PBS) and fixed with 4% Paraformaldehyde (PFA) at room temperature for 10 min. Lipids were stained with 1  $\mu$ M of Nile Red (G1264; Solarbio), and cell nuclei were stained with DAPI (ab104139; Abcam). The fluorescence intensity (DAPI: excitation wavelength/emission wavelength=405/435; Nile red: excitation wavelength/emission wavelength=555/585) was quantified and photographed under confocal microscope (Zeiss).

### Serum BPS, Lipids, and Cytokine Measurements

Mouse serum was collected and stored at  $-80^\circ\text{C}$ . The serum BPS level was measured using ultra-high performance liquid chromatography–tandem mass spectrometry (UHPLC-MS/MS) as described.<sup>30</sup> Serum level of cholesterol (CHOL), triglyceride (TG), low density lipoprotein (LDL), high density lipoprotein (HDL), nonesterified fatty acids (NEFA), alanine aminotransferase (ALT), and aspartate aminotransferase (AST) were measured by an automated biochemical analyzer (Hitachi). The cytokines were assessed using the Mouse Cytokine Panel (17 cytokines plex, EPX170-26087-901; Thermo Fisher) on Luminex (LAIZEE Biotech).

### Quantitative Real-Time PCR

Total RNA was isolated using TRIzol (15596018CN; Invitrogen). After checking the quality (Q33221; Thermo Fisher) and concentration (Q32852; Thermo Fisher) by Qubit4.0 (Q33238; Thermo Fisher), 1,000 ng RNA was reverse transcribed using HiScript III cDNA Synthesis kit (R312-01; Vazyme). Real Time Quantitative Polymerase Chain Reaction (RT-qPCR) was performed using SYBR Green (4913914001; Roche) on the LightCycler 480 system (Roche) with the following conditions: 95°C for 5 min, followed by 40 cycles of denaturation at 95°C for 10 s and annealing at 60°C for 30 s. Melt curve analyses were performed for all genes, and the specificity and integrity of the PCR products were confirmed by the presence of a single peak melt curve. The expression levels were calculated by the  $2^{-\Delta\Delta C_t}$  method, and  $\beta$ -actin was used for normalization. The sequence of the primers was listed in Excel Table S7.

### RNA-Seq and Data Analysis

RNA-seq libraries were made by TruSeq Stranded mRNA Library Prep kit (Illumina; 20020595) following library protocol from Illumina.<sup>34</sup> Briefly, total RNA was isolated and quality controlled as described above. One microgram of high-quality RNA (RNA Integrity & Quality number  $>7$ ) was used for polyA RNA enrichment and reverse transcribed to cDNA. cDNA libraries were prepared, barcoded, and amplified with the following condition: 98°C for 30 s, followed by 15 cycles of denaturation at 98°C for 10 s, annealing at 60°C for 30 s and extension at 72°C for 30 s, with a final extension at 72°C for 5 min. Then, library concentrations were measured and sequenced on NovaSeq 6000 by NovoGene.<sup>35</sup> Raw reads were trimmed to remove adaptor sequences using fastp version 0.23.1 software<sup>36</sup> and then aligned to the mouse mm10 reference genome using STAR version 2.7.10 software,<sup>37</sup> followed by quantification with the Genecode annotation file using featureCount version 2.0.2.<sup>38</sup> Differentially expression genes (DEGs) were determined using DESeq2 with false discovery rate (FDR)  $<0.05$  and  $|\log_2(\text{fold change})| \geq 0.5$ ,<sup>39</sup> and count data were Reads Per Kilobase of transcript per Million mapped reads (RPKM) normalized. GO enrichment of DEGs was performed with the ClusterProfiler version 4.2.2 package.<sup>40</sup> For the Gene Set Enrichment Analysis (GSEA), a preranked list was generated using fold change and  $p$ -values from DEGs. We then performed GSEA, using the GSEA java software and default parameters, with this list and various transcription factor targets lists (c3.tft.v7.5.1.symbols) obtained from Human MSigDB Collections (<https://www.gsea-msigdb.org/gsea/msigdb/collections.jsp>).

### ATAC-seq

The ATAC-seq libraries were prepared using Omni-ATAC protocol.<sup>41</sup> Briefly, 50K cells were pelleted, washed, and lysed in 50  $\mu$ L cold ATAC-resuspension buffer (RSB) containing 0.1% NP40, 0.1% Tween-20, and 0.01% digitonin. The lysed nuclei were washed with 1 mL of cold ATAC-RSB containing 0.1% Tween-20 but no NP40 or digitonin. Then, the nuclei were pelleted at 500 RCF for 10 min at 4°C and resuspended in 50  $\mu$ L reaction mix [25  $\mu$ L  $2 \times$  TD buffer, 2.5  $\mu$ L transposase (TD502; Vazyme), 16.5  $\mu$ L DPBS, 0.5  $\mu$ L 1% digitonin, 0.5  $\mu$ L 10% Tween-20, 5  $\mu$ L H<sub>2</sub>O] and incubated at 37°C for 30 min. DNA fragments were extracted by MinElute PCR Purification kit (28004; QIAGEN) and amplified by  $2 \times$  NEBNext Master Mix (M0541L; NEB) with Primer kit (TD204; Vazyme) using the following condition: 72°C for 5 min, 98°C for 30 s, followed by 12 cycles of 98°C for 10 s and 63°C for 30 s, and finally extension for 1 min. PCR products were purified and size selected using AMPure XP beads (A63881; Beckman Coulter). Libraries were pooled and sequenced on NovaSeq 6000 by NovoGene.

### Cleavage Under Targets and Tagmentation

Around 100K cells were collected and lysed with lysis buffer [20 mM HEPES, 10 mM KCl, 0.5 mM spermidine, 0.1% (vol/vol) Triton-X100, 20% glycerol, and  $1 \times$  Protease Inhibitor] on ice for 10 min. Then, nuclei were fixed with 0.01% formaldehyde for 2 min at room temperature and quenched by 75 mM glycine. Nuclei then were resuspended in wash buffer (20 mM HEPES, 150 mM NaCl, 0.5 mM spermidine,  $1 \times$  protease inhibitor) and mixed with concanavalin A beads (N251; NoVoNGS) in binding buffer (20 mM HEPES, 10 mM KCl, 1 mM MnCl<sub>2</sub>, and 1 mM CaCl<sub>2</sub>). The mixture was incubated with 0.5  $\mu$ L Atf3 antibody (0.811 mg/mL) (ab207434; Abcam) at 4°C overnight in 50- $\mu$ L antibody buffer [2 mM ethylenediaminetetraacetic acid (EDTA) and 0.1% (wt/vol) bovine serum albumin (BSA)]. The secondary antibody (anti-Rabbit IgG, 711-005-152; Jackson) in wash buffer (at a dilution of 1:100) was added to the mixture and



rotated at room temperature for 1 h. Then, the nuclei were washed with wash buffer and mixed with pG-Tn5 in 300  $\mu$ L wash buffer for 1 h at room temperature; 300  $\mu$ L tagmentation buffer was added to the mixture and incubated at 37°C for 1 h. To stop tagmentation, 10  $\mu$ L 0.5 M EDTA, 3  $\mu$ L 10% SDS, and 2.5  $\mu$ L 20 mg/mL Proteinase K was added to each mixture and incubated for 10 min at 70°C. Finally, DNA was extracted using the phenol chloroform method and used for amplification. Libraries were pooled and sequenced on NovaSeq 6000 by NovoGene.

### ATAC-seq and CUT&Tag Data Analysis

Raw reads were processed for adaptor trimming using fastp version 0.23.1 software,<sup>36</sup> mapped using bowtie2 version 2.3.5 to mm10<sup>42</sup> with end-to-end alignment. Deduplicated reads were marked using the Picard MarkDuplicates version 2.18.16; ENCODE blacklisted regions and mitochondrial reads were excluded, and only uniquely mapped reads with MAPQ  $\geq$  30 were retained for analysis using SAMtools version 1.17. CUT&Tag and ATAC-seq peak calling were performed with MACS3 version 3.0.0b1 with the following parameters: -f BAMPE -B -q 0.01 -extsize 200 for CUT&Tag peaks; -f BAMPE -B -q 0.01 -nomodel -shift -100 -extsize 200 for ATAC peaks. A unified peak list was determined by mergePeaks command from HOMER with more than 10 reads in at least two samples, of which the qualification of the mapped reads was performed with featureCount. Differential peaks were identified using the EdgeR or DESeq2 with a cutoff indicated in the text. Motif analysis was performed using HOMER software.<sup>43</sup> Peak annotation was performed by the ChipSeeker version 1.36.0 package using unified peak list.<sup>44</sup> The bigWig files were generated using deepTools version 3.0.2 bamCoverage command with the option: -normalizeUsing CPM. All gene transcription start sites (TSSs) were used to generate heatmaps unless specified in the text. Heatmaps and metagene plot profiles for depth normalized CUT&Tag and ATAC-seq signal were generated by deepTools.<sup>45</sup>

### Western Blot

Western blotting was performed with standard protocol. Briefly, cells were lysed in radioimmunoprecipitation assay buffer (RIPA) and centrifuged at 12,000 rpm for 10 min at 4°C. The supernatant was boiled with loading dye at 95°C for 5 min. Protein concentration was determined using a BCA Protein Quantification kit (E112-02; Vazyme), and 100  $\mu$ g protein per sample was separated by sodium dodecyl sulfate-polyacrylamide gel electrophoresis (SDS-PAGE) (120 V for 60 min) and transferred onto the polyvinylidene fluoride (PVDF) membrane (200 mA for 90 min). The membrane was then blocked with 5% skim milk at room temperature for 1 h and incubated at 4°C overnight with the Atf3 (CST; 33593), Gapdh (CST; 5174), and Actb (Affinity; AF7018) at a dilution of 1:1,000. After washing with PBST, the membrane was incubated with anti-Rabbit IgG (A0208; Beyotime) at a dilution of 1:1,000 at room temperature for 1 h. The signal was then detected with ECL substrates (FD8000; Fdbio Science) on Tanon-2500 (Tanon). The signal was quantified by ImageJ software (NIH).

**IP-MS and Co-IP.** For immunoprecipitation (IP), cells were washed and lysed using IP buffer (Beyotime; P0013) containing 1 mM phenylmethylsulfonyl fluoride (PMSF) (Beyotime; ST507). After centrifugation at 12,000  $\times$  g for 10 min, the supernatant was collected. The lysates were precleared by incubating with 30  $\mu$ L IP buffer-washed protein A&G magnetic beads (Vazyme; PB101) for 1 h at 4°C. Five micrograms Anti-ATF3 antibody (Abcam; ab207434) or IgG XP Isotype Control (CST; 3900S) was added to each lysate and incubated overnight at 4°C. On the second day, each sample was incubated with 30  $\mu$ L IP buffer-washed protein A&G magnetic beads for another 4 h at

4°C. After incubation, the beads were washed three times with cold PBST and boiled in 2 $\times$  SDS loading buffer for 10 min. The processed IP samples were used in western blotting, Co-IP, and IP-MS. The IP-MS was done at Westlake Omics (Westlake Omics).

**Overexpression Atf3 in knockout cells.** Atf3 coding sequence (provided in Excel Table S4) was amplified from cDNA of the AML12 cell line (forward primer: 5'-cggaattctatgatgcttcaacaccagggc-3'; reverse primer: 5'-cgcgaaatccttagctctgcaatgttcctt-3') using the following conditions: 95°C for 3 min, 35 cycles at 95°C for 10 s, 56°C for 30 s and 68°C for 30 s, with a final extension at 68°C for 5 min. The PCR products were sent to Novogene for verification by Sanger sequencing. The pCDH-CMV vector (72265; Addgene) was digested at 37°C overnight using *EcoRI/BamHI* (Thermo Fisher; FD0274/FD0054), and then Atf3 cDNA was ligated into digested vector backbone using T4 DNA ligase (2011A; TaKaRa) at 16°C overnight. The day before transfection, 6  $\times$  10<sup>5</sup> Atf3 knockout cells were seeded on 6-cm dishes. Atf3 was reexpressed in knockout cells by transfecting cells with pCDH-CMV-Flag-Atf3 vector using Lipo3000 (Thermo Fisher; L3000015) according to the manufacturer's instructions. Transfected cells were cultured for 48 h, and western blotting was used to detect ATF3 protein level.

### Immunofluorescence

AML12 cells were seeded in confocal dishes (Biosharp; BS-CP-6B). After BPS exposure, cells were fixed with 4% formaldehyde for 15 min at room temperature and permeabilized with 0.1% TritonX-100 for 10 min at room temperature. To minimize background signal, a blocking buffer (2% BSA and 22.5 mg/mL glycine in PBST) was applied. The cells were then incubated overnight at 4°C with ATF3 antibody (Abcam; ab207434) diluted 1:100. The next day, the secondary antibody (Beyotime; P0179) diluted 1:1,000 was added and incubated at room temperature for 1 h with gentle rotation. Nuclei were stained with DAPI (Abcam; ab104139), and fluorescence intensity was captured using a confocal microscope (Zeiss).

### Statistical Analysis

All statistical analyses were performed by two-tailed Student's *t* test, Mann-Whitney U test, or chi-squared test using GraphPad Prism 8 (GraphPad, 8.0, Motulsky, USA) and RStudio (Posit, 4.3.0, USA). The level of significance was set at *p* < 0.05 and indicated as follows: \**p* < 0.05; \*\**p* < 0.01; \*\*\**p* < 0.001; \*\*\*\**p* < 0.0001. All data were expressed as means  $\pm$  standard error of the mean (SEM).

## Results

### Body Weight, Lipids Deposition, and Transcriptome in Mice and AML12 Cells Exposed to BPS

To understand whether BPS affects hepatic lipid metabolism, we exposed mice to different doses of BPS for 12 weeks. There were no significant differences in body weight gain and liver organ coefficient (liver mass/body weight  $\times$  100%) between the BPS and control groups (Figure 1A,B). We further analyzed the serum level of cholesterol (CHOL), triglyceride (TG), low-density lipoprotein (LDL), high-density lipoprotein (HDL), nonesterified fatty acids (NEFA), alanine aminotransferase (ALT), and aspartate aminotransferase (AST) and found LDL, NEFA, and ALT levels were significantly higher in BPS groups compared to control (Figure 1C; Figure S1A) (LDL and NEFA in both BPS groups and ALT in only the low-dose group, 0.1 mg/kg/day). Besides, H&E and Oil Red O staining showed a significantly larger area of intracellular lipid droplet accumulation in the BPS group compared to control (Figure 1D,E). Using the Mouse Cytokine Panel, we measured serum cytokines

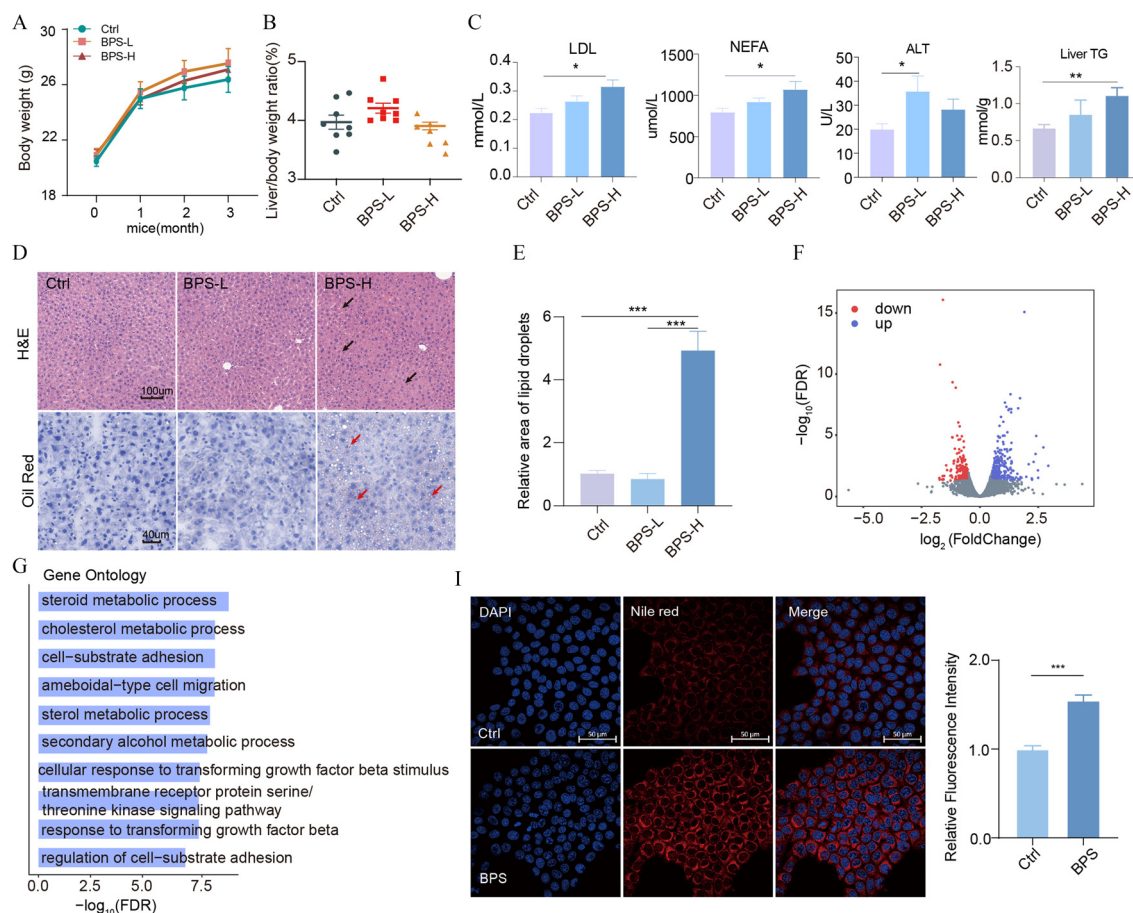


**Figure 1.** Body weight, serum lipids, histology, and transcriptome in mice or AML12 cells after BPS exposure. (A) Body weight (mean and SEM) of study animals (eight mice per group) in the control, BPS-L (0.1 mg/kg BW/day), and BPS-H (1 mg/kg BW/day) group, respectively. (B) Liver/body weight ratio (mean and SEM, seven to eight mice per group) in the control, BPS-L, and BPS-H group, respectively. (C) Low-density lipoprotein (LDL), nonesterified fatty acids (NEFA), and alanine aminotransferase (ALT) in the control, BPS-L, and BPS-H group, respectively (seven to eight mice per group). (D) Hematoxylin and eosin (H&E) staining and Oil Red O staining of liver in the control, BPS-L, and BPS-H group, respectively. Arrows indicated the area of intracellular lipid droplet. (E) Quantification of Oil Red O staining positive area by ImageJ. (F) Volcano plot and heatmap of BPS-H-associated differentially expressed genes in mice. (G,H) Gene Ontology and KEGG analysis of differentially expressed genes in the control and BPS-H group. (I) Nile Red staining of AML12 cells in control and BPS (100  $\mu$ M) group. (J) Nile Red staining of mouse primary hepatocytes in control and BPS (100  $\mu$ M) group. (K) Volcano plot and heatmap of differentially expressed genes in AML12 cells treated with control vs. BPS (100  $\mu$ M). (L) Gene Ontology analysis of differentially expressed genes between AML12 cells treated with control vs. 100  $\mu$ M BPS. (M) Heatmap of 18 metabolism-related pathways in Gene Ontology analysis. Data in this figure are also presented in Excel Table S1. Note: All of the column graphs depict mean and SEM. Significance was calculated using nonpaired two-tailed Student's *t* test. \**p*  $\leq$  0.05; \*\**p*  $\leq$  0.01; \*\*\**p*  $\leq$  0.001; and \*\*\*\**p*  $\leq$  0.0001. BPS, bisphenol S; BPS-H, (1 mg/kg BW/day); BPS-L, (0.1 mg/kg BW/day); BW, body weight; Ctrl, control; FDR, false discovery rate; SEM, standard error of the mean.

and observed significantly lower levels of interleukin 9 (IL9), IL10, and IL27 after BPS (high dose group, 1 mg/kg/day) exposure (Figure S1F). Sirius Red stain indicated slightly more fibrosis in both BPS exposure groups, but this did not reach statistical significance (Figure S1G).

Next, we performed RNA-seq (two animals per group) to identify transcriptional changes after BPS exposure. Totally, 567 genes were dysregulated, including 351 upregulated genes and 216 downregulated genes (Figure 1F; Figure S1B) in BPS vs. control groups. These differentially expressed genes (DEGs) were reflective of altered metabolic processes in liver after BPS exposure. Gene Ontology (GO) analysis indicated that dysregulated genes were involved in pathways including the steroid metabolic process, cholesterol metabolic process, and steroid biosynthetic process (Figure 1G). KEGG analysis showed that nonalcoholic fatty liver disease related pathway was the top enriched pathway (Figure 1H).

AML12 cells were utilized to elucidate the detailed mechanism of BPS-mediated disturbance of lipid metabolism. We first evaluated

cell proliferation across a range of BPS (0.01  $\mu$ M–100  $\mu$ M) exposure over 24 h. We found no significant differences in proliferation at any concentrations used (Figure S1C); we, therefore, used 100  $\mu$ M in the study. Interestingly, we observed significantly greater deposition of lipids in the BPS exposure group (Figure 1I), which was consistent with what we observed in mice (Figure 1D,E). In addition, we exposed mouse primary hepatocytes to BPS (100  $\mu$ M, 24 h) and observed the similar phenotype (Figure 1J). As expected, compared with the control group, BPS exposure cells (three biological replicates per group) had 2,138 DEGs (955 upregulated and 1,183 downregulated genes) (Figure 1K; Figure S1D). GO analysis indicated that enriched pathways were related to metabolism including steroid metabolic, steroid biosynthetic, and fatty acid metabolic processes (Figure 1L). Hallmark genes in *de novo* lipogenesis (*Elovl6* and *Scd1*) were all downregulated in BPS cells vs. control. We also observed upregulation of fatty acid metabolism-related genes. For example, the type one acyl-CoA thioesterase, *Acot2*, was more highly expressed in the BPS-treated cells. Likewise, other up-regulated genes were associated with fatty acids oxidation, such as

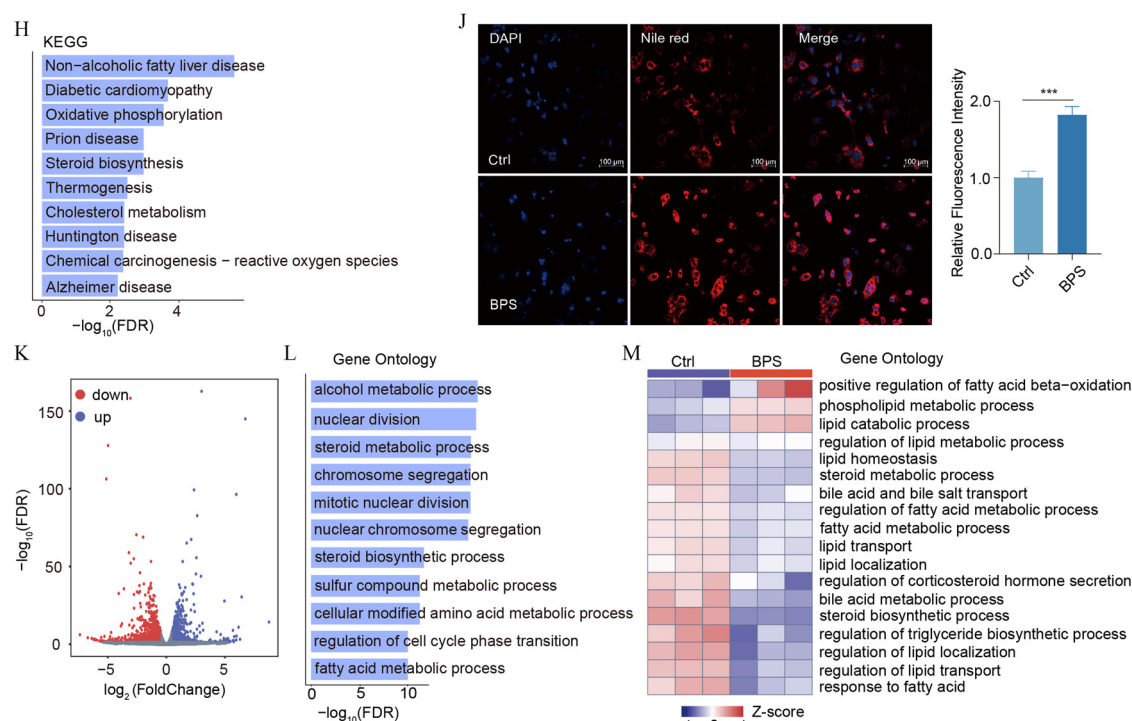


**Figure 1.** (Continued.)

*Acox2*, *Acaa1*, and *Cpt1*. A subset of DEGs was validated by qPCR (Figure S1E). To determine how lipid metabolism was affected by BPS, we clustered a total of 18 pathways related to metabolism in GO analysis. As expected, for most lipid biosynthetic pathways, associated genes were expressed at a lower level in BPS-exposed cells (Figure 1M).

### Chromatin Accessibility in AML12 Cells Exposed to BPS

Chromatin accessibility broadly refers to the level of openness in certain genomic regions, where transcription factors bind and regulate gene expression. To evaluate the impact of BPS on open chromatin, we measured chromatin accessibility in AML12 cells with or without BPS treatment using ATAC-seq (two biological replicates per group). We determined differences in accessibility between treatments using EdgeR ( $FDR < 0.05$ ,  $|\text{fold change}| > 1.5$ ), finding that 2,632 loci exhibited differential accessibility after BPS exposure (Figure 2A). Among them, 1,427 exhibited more accessibility and 1,205 exhibited less accessibility (Figure 2B). A depiction of differentially accessible loci is presented in Figure 2C. The majority of differentially accessible regions were located in distal regions rather than proximal to transcription start sites (TSS) across the genome (Figure 2D,E). As expected, GO analysis indicated that regions with different ATAC signals were enriched with genes associated with metabolism, including the alcohol metabolic process, sterol metabolic process, and cholesterol metabolic process (Figure 2F), which is also consistent with the *in vivo* and *in vitro* phenotype of BPS exposure. We next asked whether BPS-remodeled open chromatin regions have a regulatory role in gene expression. We assigned nearest DEGs to differentially accessible loci and found that DEGs near loci with increased accessibility had significantly higher expression than those with decreased accessibility (Figure 2G).

In order to understand the enrichment of binding sequences for transcription factors at differentially accessible regions, we performed Homer motif analysis. Interestingly, the top enriched binding motifs corresponded to bZIP (Atf3, FOS, Fra1, and JunB) family transcription factors (Figure 2I). Among all ATF

family members, we also found that only Atf3 was significantly upregulated after BPS exposure (Figure 2J). Consistent with our hypothesis, gene set enrichment analysis showed enrichment of *Atf3* in DEGs (Figure 2K). Thus, in the following study, we focused on the function of Atf3 in lipid metabolism.

### Genome-Wide Localization of Atf3 in AML12 Cells Exposed to BPS

To determine the genome-wide localization of Atf3 and how it responds to BPS exposure, we performed cleavage under targets and tagmentation (CUT&Tag) in AML12 cells before and after BPS treatment (three biological replicates per group). Atf3 peaks were called by MACS and showed a significant overlap across biological replicates, regardless of group. As presented in Figure 3A, we found Atf3 binding signal at gene TSS was significantly upregulated (Figure 3A,B). A depiction of Atf3 binding is presented in Figure 3C,D. Totals of 8,295 and 10,811 ATF3 binding sites in the control group and BPS group, respectively, were located in promoter regions (Figure 3E). As for the distance to the TSS, over 40% peaks were located more than 50 kb away from TSS (Figure 3F), which suggested that Atf3 might also bind to enhancer regions. Totally, we identified 2,232 Atf3 differential binding sites ( $FDR < 0.05$ ; 1,338 peaks with gained signal and 894 peaks with lost signal) (Figure 3G,H). We observed that Atf3 binding was higher at sites with increased accessibility and lower at sites with decreased accessibility (Figure 3G,H). An example of a differentially bound peak is presented in Figure 3I. When we annotated the location of differentially bound peaks, we found that 343 gained peaks and 476 lost peaks were located at distal intergenic regions (Figure 3J,K).

To interrogate the biology under these differential binding regions, we carried out GO analysis. The results indicated that those regions were enriched with genes involved in pathways including positive regulation of protein metabolic process, anatomical structure formation involved in morphogenesis, negative regulation of signal transduction, and so on (Figure 3L). Targeted



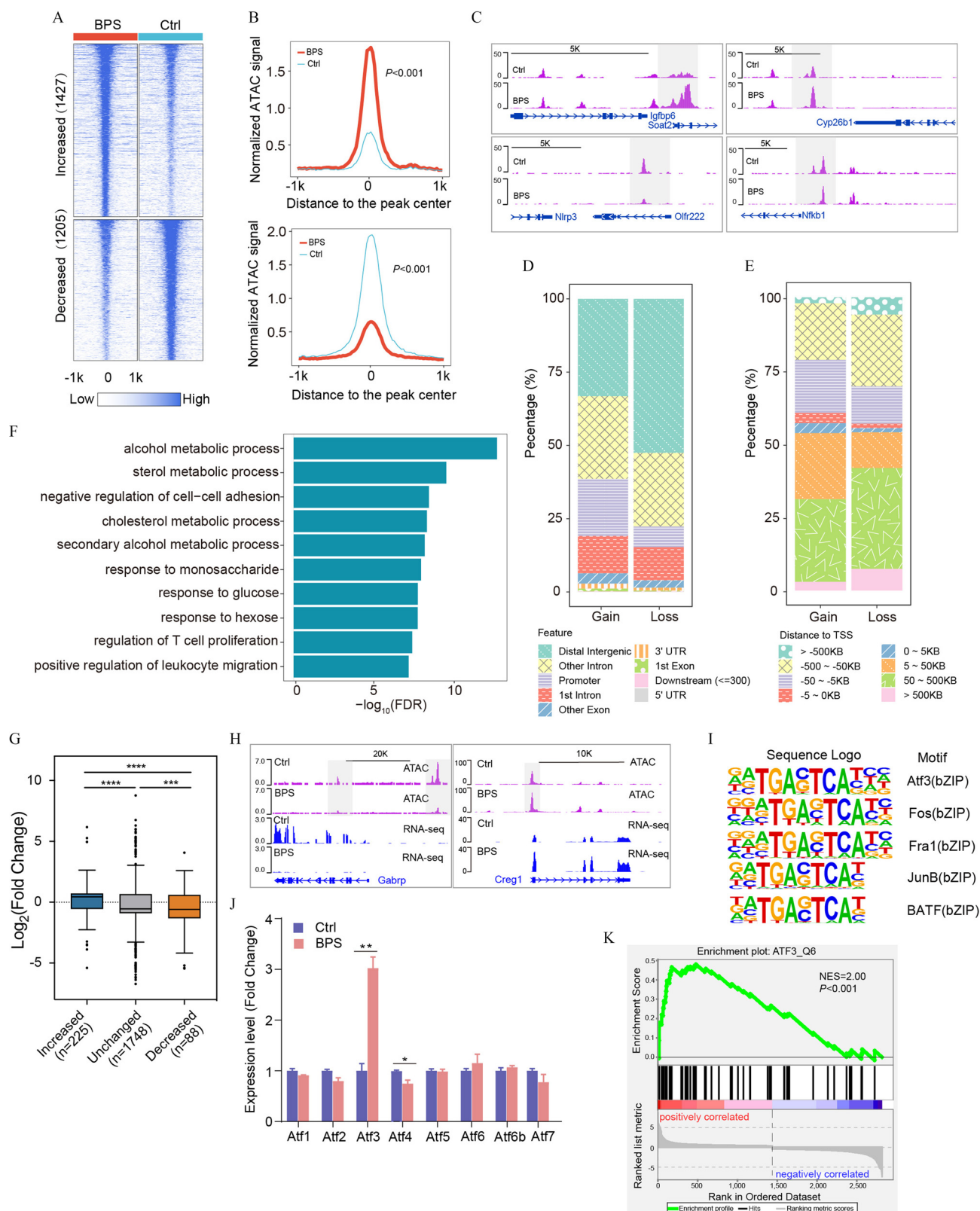


**Figure 2.** Chromatin accessibility in AML12 cells after BPS exposure. (A) Heatmap of differential chromatin-accessible regions (two biological replicates per group) in control (Ctrl) and BPS (100  $\mu$ M) groups. (B) Metagenes plot of ATAC signal at differential chromatin-accessible regions. (C) Examples of differential chromatin-accessible regions near gene promoters. (D,E) Annotation of differential chromatin-accessible regions. (F) Gene Ontology analysis of differential chromatin-accessible regions. (G) Box plots showing differential gene expression as a function of differential chromatin-accessible regions near a transcription start sites (TSS) ( $\pm 100$  kb). Box denotes 25th to 75th percentile; horizontal bar is median. Significance was calculated using Mann-Whitney U test. (H) Examples of differentially expressed genes with differential chromatin-accessible regions. (I) Motifs enriched at differential chromatin accessible regions. (J) Expression levels of ATF family genes in control and BPS group. The column graph depicts mean and SEM. Significance was calculated using nonpaired two-tailed Student's *t* test. (K) GSEA of differentially expressed genes. Data in this figure were also presented in Excel Table S2. Note: \* $p \leq 0.05$ ; \*\* $p \leq 0.01$ ; \*\*\* $p \leq 0.001$ ; \*\*\*\* $p \leq 0.0001$ . ATAC, assay for transposase-accessible chromatin; ATF, activating transcription factor; BPS, bisphenol S; FDR, false discovery rate; GSEA, Gene Set Enrichment Analysis; UTR, untranslated region.





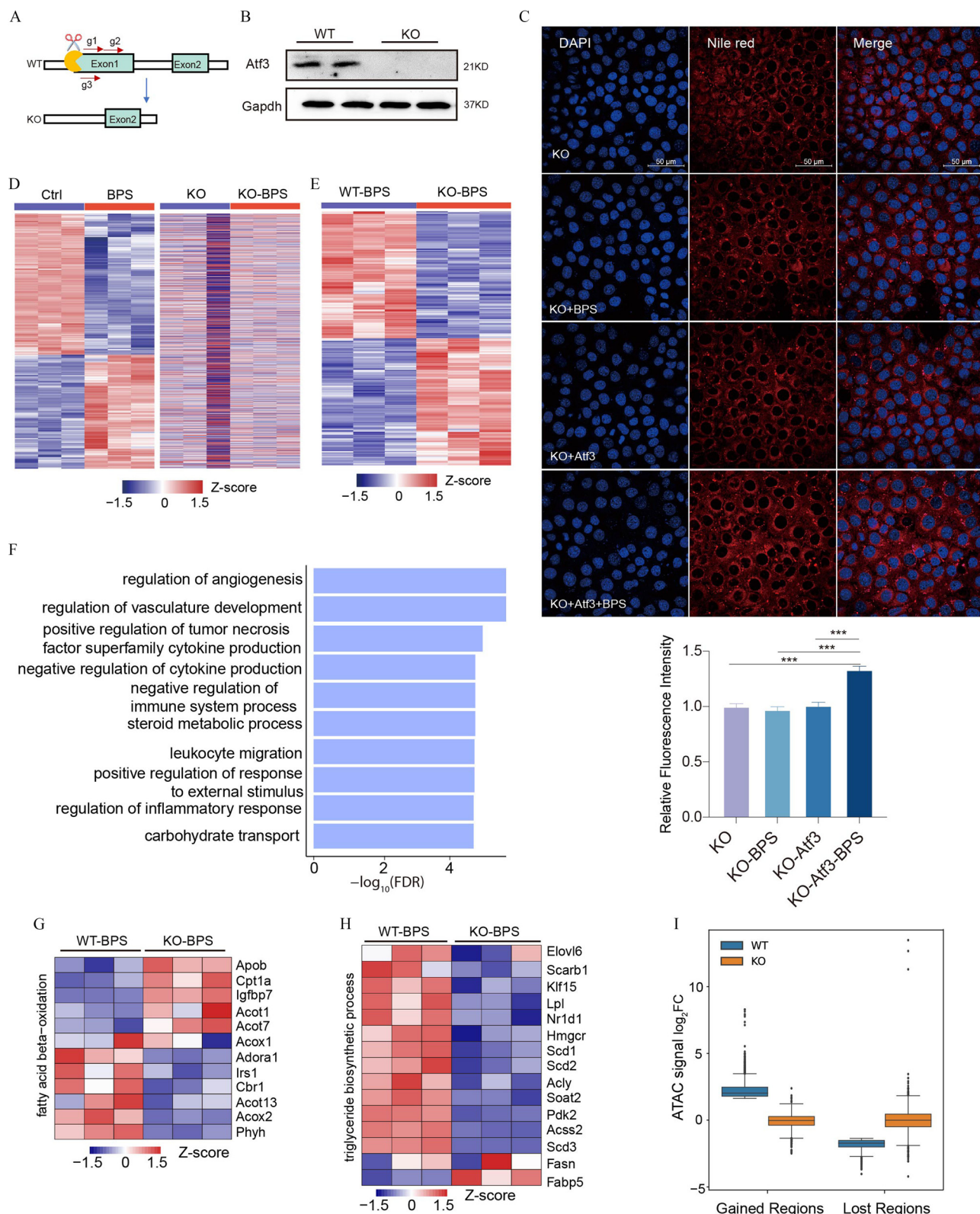


**Figure 4.** Lipid deposition, transcriptome, and chromatin accessibility in wild-type and *Atf3* knockout cells after BPS exposure. (A) Schematic overview of *Atf3* knockout (KO) strategy by CRISPR/Cas9. (B) Western blot validation of *Atf3* KO efficiency in AML12 cell line. (C) Nile Red staining of wild-type (WT) and *Atf3* KO cells after BPS (100  $\mu$ M) treatment. (D) The heatmap depicts expression of genes dysregulated in WT cells after BPS treatment compared to control adjacent to the same genes in *Atf3* KO cells. (E) Heatmap of differentially expressed genes in WT and *Atf3* KO cells after BPS exposure. (F) Gene Ontology analysis of differentially expressed genes. (G,H) Heatmap of key genes involved in fatty acids oxidation or in triglyceride biosynthetic process. (I) Box plots showing ATAC signal fold differences at gained and lost accessibility regions as identified in the WT cells after BPS exposure compared to control. Box denotes 25th to 75th percentile, horizontal bar is median, whiskers extend to  $1.5 \times \text{IQR}$  beyond the box. Data in this figure were also presented in Excel Table S4. Note: ATAC, assay for transposase-accessible chromatin; BPS, bisphenol S; Ctrl, control; IQR, interquartile range.

to these regions, we used Homer motif to obtain potential TFs, and the enriched motifs corresponded to the ATF3 binding sequences (Figure 3M).

### **Transcriptome and Chromatin Accessibility in Atf3 Knockout Cells Exposed to BPS Knockout of Atf3 Mitigates BPS-Induced Lipid Deposition**

To understand Atf3's function in lipid deposition, we knocked out Atf3 in AML12 cells using CRISPR/Cas9 (Figure 4A). Western blot showed significantly lower expression of Atf3 (Figure 4B). There was no significant difference in lipid accumulation between wild type (WT) and Atf3 knockout cells without BPS exposure (Figure S1H). We examined the fluorescence intensity of Nile red in Atf3 knockout cell with BPS exposure and found the lipid deposition was attenuated compared with the control (Figure 4C). We first assessed the effects of deleting Atf3 on BPS-induced gene expressions. A heatmap was generated showing genes exhibiting BPS-induced dysregulation in wild-type cells with the same genes depicted from Atf3 knockout cells (Figure 4D). The Atf3 knockout cells showed a completely different expression pattern of these genes than did wild-type cells (Figure 4D). We next compared the gene expression differences (three biological replicates per group) in Atf3 knockout cells before and after BPS exposure. Using the same cutoff, there were only 11 DEGs (Figure S1I,J).

Using Atf3 knockout cells, we asked how gene expression changes under BPS exposure without Atf3 (WT-BPS, KO-BPS). Compared with WT-BPS, there were 396 DEGs, including 198 upregulated DEGs and 198 regulated DEGs (Figure 4E). GO ontology analysis of these DEGs showed the enrichment of steroid metabolic process, positive regulation of response to external stimulus, and so on (Figure 4F). Next, we examined expression of genes in fatty acid oxidation and triglyceride biosynthetic process in our data, observing that Atf3 KO cells exposed to BPS exhibited a lower expression of genes related to lipogenesis as compared with WT-BPS (Figure 4G,H). Comparison of ATAC-seq data collected from AML12 WT and Atf3 KO cells demonstrated that regions with BPS induced accessibility changes did not differ significantly without Atf3 (Figure 4I).

### **Transcriptome and Chromatin Accessibility in Atf3 LKO Mice Exposed to BPS**

To examine whether Atf3 modulates hepatic lipids metabolism *in vivo*, we generated the Atf3<sup>fx/fx</sup> and hepatic Atf3 knockout mice (Atf3 LKO) (Figure 5A,B). We exposed the Atf3 LKO mice to BPS for 3 months and recorded the mice weight (Figure 5C). Pathology results suggested less lipid deposition in Atf3 LKO group compared to Atf3<sup>fx/fx</sup> group (Figure 5D,E). Partially due to high variation between mice, we did not observe significant differences in cytokine IL9, IL10, and IL27 between the control and BPS group, which were previously seen in wild-type mice (Figure S2A). We found differences in cytokine interferon-gamma (IFN-gamma), tumor necrosis factor-alpha (TNF-alpha), and granulocyte-macrophage colony-stimulating factor (GM-CSF) between the control and BPS group in Atf3 KO mice (Figure S2A). We next assessed transcript abundance (two biological replicates per group) in Atf3 LKO mice after BPS treatment finding only six DEGs (Figure S2B,C). We generated a heatmap showing genes with BPS-induced dysregulation in WT mice with the same genes exhibited from Atf3 LKO mice (Figure 5F). The Atf3 LKO mice showed a different gene expression pattern from WT mice (Figure 5F).

To clarify the direct regulatory capacity of BPS on chromatin accessibility in an Atf3 LKO mouse, we carried out ATAC-seq

in Atf3 LKO mouse liver (two biological replicates per group). In agreement with gene expression differences, differential chromatin accessibility around gene TSS was generally attenuated without Atf3 (Figure 5G,H). Examples for Atf3 binding and chromatin accessibility are presented in Figure 5I, where the sterol O-acyltransferase Soat2 exhibit alterations after BPS exposure depending on Atf3 binding at chromatin-accessible regions. Although we also observed chromatin accessibility differences in BPS vs. control mice, we did not find enrichment of the Atf3 binding motif (Figure S2D–H).

Atf3 was localized in cellular nucleus and upregulated after BPS exposure (Figure 6A). To reveal the cofactors of Atf3, we performed co-immunoprecipitation-mass spectrometry (IP-MS). In total, we identified 568 potential target proteins. Through overlap analysis using DEGs and motifs from CUT&Tag and ATAC-seq, we observed JunB and JunD as the Atf3 cofactors (Figure 6B). JunB has the similar motif with Atf3 (Figure 6C) and was upregulated in the BPS group (Figure 6D). Co-IP showed interactions of Atf3 with JunB. JunB was also upregulated in AML12 cells, primary hepatocytes and liver tissues in the BPS group compared to control (Figure 6E–H). Next, we used SR11302 to inhibit the AP-1 activity and observed the downregulation of JunB and Atf3 level, while overexpression of Atf3 did not increase the JunB level (Figure 6I–K). Besides, inhibiting AP-1 attenuated BPS-induced lipid accumulation in AML12 cells (Figure 6L,M). Taken together, our proposed model is presented in Figure 6N.

## **Discussion**

MASLD is part of an emerging epidemic of metabolism-based pathologies and is considered present when ≥5% of the hepatocytes become fat filled. The pathophysiology of MAFLD is highly complex, including metabolic disturbance, chronic inflammation, and fibrosis.<sup>46</sup> Here, we demonstrated that animals exposed to BPS for chronic periods exhibited cellular and molecular alterations associated with MASLD. BPS-exposed animals exhibited obvious lipid deposition in the liver, which was accompanied by dramatic transcriptome differences from control animals. Our findings illustrated the capacity of BPS exposure to result in chromatin accessibility alterations downstream of the signal responsive factor Atf3 reflected in altered gene expression (Figure 5J).

BPS had been reported to affect lipid metabolism *in vitro*<sup>47,48</sup> and *in vivo*,<sup>49,50</sup> while our knowledge on its molecular mechanism is scarce. BPS was shown to induce lipid accumulation through activating Pparγ in preadipocytes.<sup>48</sup> In contrast to the observations in adipocytes, we observed that chromatin accessibility dynamics, including Atf3 localization, were dramatically altered in hepatocytes and liver after BPS exposure. It raises opportunities to discern the underlying transcriptional regulatory networks. To determine whether chromatin accessibility differs after BPS exposure, differences in open chromatin regions were analyzed by ATAC-seq. Surprisingly, open chromatin regions were broadly similar after BPS exposure, suggesting that a baseline chromatin landscape was stable. Interestingly, we still observed several thousand altered accessible regions after BPS exposure, which can be used to bind by stress responsive transcription factors, such as ATF3.

ATF3 is a stress-responsive transcription factor and belongs to ATF/CREB protein family. It contains a leucine zipper structure that regulates transcription through forming dimers.<sup>51</sup> Such regulation might be facilitated by creating open chromatin for cofactors. ATF3 was functional as a stress-responsive network hub of the cell and could be activated by extracellular signals including endoplasmic reticulum stress, cytokines, and so on.<sup>52</sup> Recent studies indicated that ATF3 was involved in glucose metabolism in the pancreas, liver, adipose tissue, hypothalamus, and



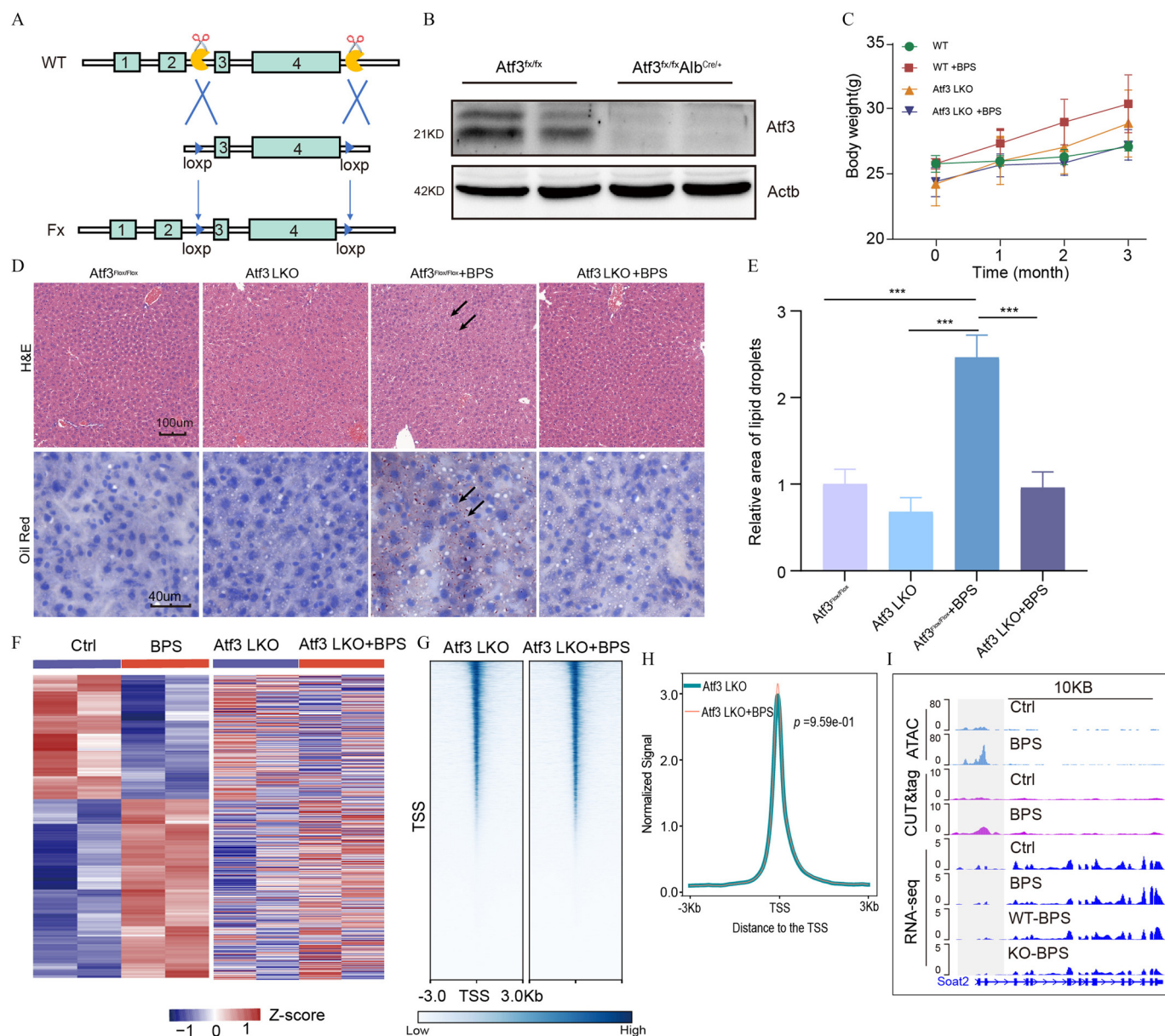


**Figure 5.** Body weight, histology, transcriptome, and chromatin accessibility in wild type and *Atf3* knockout mice after BPS exposure. (A) Schematic overview of generation of *Atf3* knock out (KO) mice. (B) Western blot validation of liver *Atf3* KO (LKO) efficiency in mice. (C) Body weight (mean and SEM) of mice in WT and LKO group (four mice per group) with/without BPS (1 mg/kg BW/day) exposure for 12 wk. (D) Hematoxylin and eosin (H&E) staining and Oil Red O staining of liver in WT and LKO group with/without BPS exposure. (E) Quantification of Oil Red O staining—positive area by ImageJ. (F) The heatmap depicts expression of genes dysregulated in WT mice exposed to BPS compared to control adjacent to the same genes in *Atf3* LKO mice. (G) Heatmap and metagene plot of ATAC signal at all gene TSSs. (H) Metagene plot of ATAC signal at all gene TSSs. (I) Example of *Atf3* binding at promoter regions to regulate gene expressions after BPS exposure. Data in this figure were also presented in Excel Table S5. Note: ATAC, assay for transposase-accessible chromatin; BPS, bisphenol S; BW, body weight; Ctrl, control; SEM, standard error of the mean; TSS, transcription start site; WT, wild type.

heart.<sup>52</sup> It repressed the expression of genes encoding gluconeogenic enzymes in the liver in a mouse model.<sup>53</sup> Our data also suggest that *Atf3* promoted lipid deposition and regulated serum cytokines in mice. We observed the upregulation of genes reported to promote MASLD, including *Soat2* and *Pdk2*. *Soat2* encodes acyl-coenzyme A: cholesterol acyltransferase 2 (ACAT2), which played key roles in synthesizing cholesteryl esters in hepatocytes and very-low-density lipoprotein (VLDL) secretion.<sup>54</sup> Inhibition of ACAT2 improves liver steatosis and hypercholesterolemia in mice.<sup>54,55</sup> Previous studies also suggested that *Atf3* played a dual role in regulating of inflammatory responses in mice.<sup>56–58</sup> We found *Atf3* was associated with both anti-inflammatory and proinflammatory gene expression during BPS exposure.

The activator protein-1 (AP-1) transcription factor is involved in multiple cellular and physiological functions and can be activated by hormones, stresses, cytokines, and inflammation.<sup>59</sup> AP-1 is often defined as the dimers made up of the “Fos-” and “Jun proteins.”<sup>59</sup> JunB is one of the key components of AP-1.<sup>59</sup> Our data suggest that *Atf3* was interacted and regulated by JunB (Figure 6). In addition, it suggests that inhibition of AP-1/JunB downregulated the BPS-induced *Atf3* expression, while inhibiting *Atf3* did not affect AP-1/JunB.

In contrast to our results, Xu et al. reported overexpression of human ATF3 in hepatocytes prevented steatohepatitis in ob/ob [*Lep*<sup>ob/ob</sup>, mice with homozygous mutations in the (Leptin, *Lep*) gene] and db/db [*Lepr*<sup>db/db</sup>, mice with homozygous mutations in



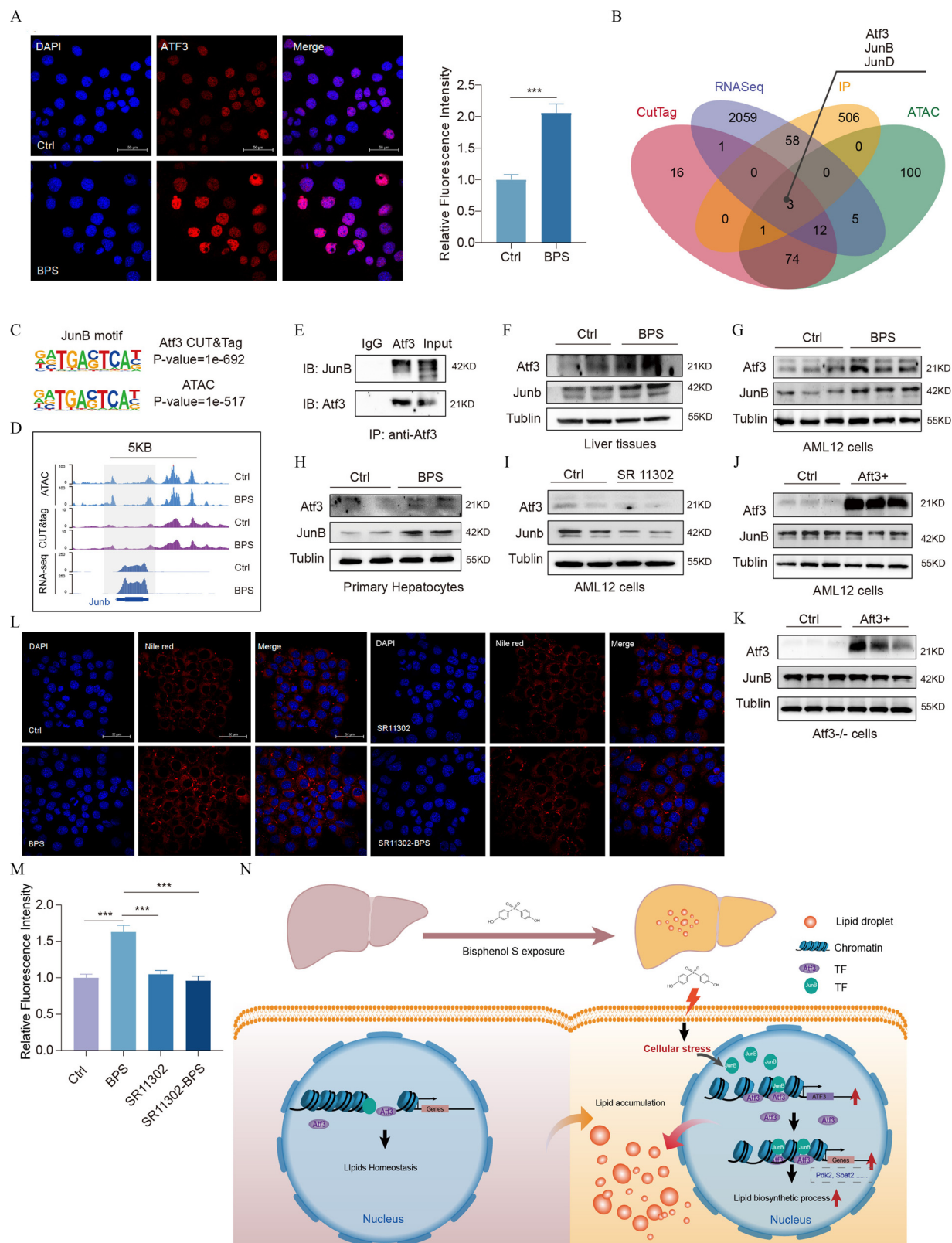


**Figure 6.** Immunoblots of Atf3 and JunB in mouse primary hepatic cell, mouse liver tissue, and AML12 cell after BPS exposure. (A) ATF3 staining in AML12 cells in control and BPS (100  $\mu$ M) group. (B) Overlap analysis between ATF3 CUT&Tag motifs, ATAC motifs, RNA-seq DEGs, and IP-MS proteins. (C) Example of JunB motif. (D) Example of Atf3 binding signal and chromatin accessibility near JunB. (E) IP-WB of ATF3 and JunB. (F–H) WB of ATF3 and JunB in mouse liver tissue, mouse primary hepatocytes, and AML12 cells. (I) WB of ATF3 and JunB in AML12 cells after SR11302 treatment. (J) WB of ATF3 and JunB in AML12 cells after ATF3 overexpression. (K) WB of ATF3 and JunB in ATF3 knockout AML12 cells after ATF3 overexpression. (L) Nile Red staining of AML12 cells in the control, BPS (100  $\mu$ M), and BPS+SR11302 group. (M) Quantification of fluorescence intensity of Nile Red staining in Figure 6L. (N) Schematic representation of the mechanistic model. The numeric data are provided in Excel Table S6. Note: ATAC, assay for transposase-accessible chromatin; BPS, bisphenol S; Ctrl, control; CUT&Tag, cleavage under targets and tagmentation; DEG, differentially expression genes; IP, immunoprecipitation; MS, immunoprecipitation; WB, western blot.

the Leptin receptor (Lepr) gene] mice through inducing hepatic lipolysis and fatty acid oxidation.<sup>60</sup> Our RNA-seq data also showed the upregulation of lipid metabolism genes and down-regulation of lipogenesis genes after BPS exposure. One possibility was the chemical-induced model in our study is different from their diet-induced model.

In summary, our study offered new knowledge about how chromatin accessibility and the transcriptional network respond to environmental cues. We unveiled that BPS exposure shaped the chromatin landscape and upregulated Atf3 to regulate genes involved in lipid synthesis and catabolism, leading to hepatic lipid deposition. Therefore, our findings provide a novel mechanistic connection between BPS exposure and hepatic lipid deposition and suggest that inhibition of ATF3 reduced susceptibility to hepatic diseases.

## Acknowledgments

This work was supported by the National Natural Science Foundation of China (82173548, 82173550, 82304094, 82173536), Innovative and Entrepreneurial Team of Jiangsu Province (JSSCTD202144), the Natural Science Foundation of Jiangsu Province of China (BK20220317), and the Intramural Research Program of the NIEHS, NIH (ES101965 to P.A.W.). Y.Q. is a Jiangsu specially-appointed professor.

Sequencing data that support the findings of this study have been deposited in National Genomics Data Center with the following accession number PRJCA023648 (<https://ngdc.cncb.ac.cn/bioproject/browse/PRJCA023648>). All other relevant data supporting the key findings are available within the supplementary data or from the corresponding author upon reasonable request.

## References

- Younossi ZM. 2019. Non-alcoholic fatty liver disease – a global public health perspective. *J Hepatol* 70(3):531–544, PMID: 30414863, <https://doi.org/10.1016/j.jhep.2018.10.033>.
- Li J, Zou B, Yeo YH, Feng Y, Xie X, Lee DH, et al. 2019. Prevalence, incidence, and outcome of non-alcoholic fatty liver disease in Asia, 1999–2019: a systematic review and meta-analysis. *Lancet Gastroenterol Hepatol* 4(5):389–398, PMID: 30902670, [https://doi.org/10.1016/S2468-1253\(19\)30039-1](https://doi.org/10.1016/S2468-1253(19)30039-1).
- Leslie T, Pawloski L, Kallman-Price J, Escheik C, Hossain N, Fang Y, et al. 2014. Survey of health status, nutrition and geography of food selection of chronic liver disease patients. *Ann Hepatol* 13(5):533–540, PMID: 25152986.
- Sveinbjornsson G, Ulfarsson MO, Thorolfsson RB, Jonsson BA, Einarsson E, Gunnlaugsson G, et al. 2022. Multiomics study of nonalcoholic fatty liver disease. *Nat Genet* 54(11):1652–1663, PMID: 36280732, <https://doi.org/10.1038/s41588-022-01199-5>.
- Chen Y, Wang Y, Cui Z, Liu W, Liu B, Zeng Q, et al. 2023. Endocrine disrupting chemicals: a promoter of non-alcoholic fatty liver disease. *Front Public Health* 11:1154837, PMID: 37033031, <https://doi.org/10.3389/fpubh.2023.1154837>.
- Peng J, Du LL, Ma QL. 2023. Serum glycolipids mediate the relationship of urinary bisphenols with NAFLD: analysis of a population-based, cross-sectional study. *Environ Health* 21(1):124, PMID: 36588154, <https://doi.org/10.1186/s12940-022-00945-w>.
- Wang Q, Li D, Cao G, Shi Q, Zhu J, Zhang M, et al. 2021. IL-27 signalling promotes adipocyte thermogenesis and energy expenditure. *Nature* 600(7888):314–318, PMID: 34819664, <https://doi.org/10.1038/s41586-021-04127-5>.
- Hong T, Zou J, He Y, Zhang H, Liu H, Mai H, et al. 2023. Bisphenol A induced hepatic steatosis by disturbing bile acid metabolism and FXR/TGR5 signaling pathways via remodeling the gut microbiota in CD-1 mice. *Sci Total Environ* 889:164307, PMID: 37211107, <https://doi.org/10.1016/j.scitotenv.2023.164307>.
- Wang J, Yu P, Xie X, Wu L, Zhou M, Huan F, et al. 2021. Bisphenol F induces nonalcoholic fatty liver disease-like changes: involvement of lysosome disorder in lipid droplet deposition. *Environ Pollut* 271:116304, PMID: 33401208, <https://doi.org/10.1016/j.envpol.2020.116304>.
- Chen D, Kannan K, Tan H, Zheng Z, Feng Y-L, Wu Y, et al. 2016. Bisphenol analogues other than BPA: environmental occurrence, human exposure, and toxicity-a review. *Environ Sci Technol* 50(11):5438–5453, PMID: 27143250, <https://doi.org/10.1021/acs.est.5b05387>.
- Mustieles V, Rolland M, Pin I, Thomsen C, Sakhi AK, Sabaredzovic A, et al. 2023. Early-life exposure to a mixture of phenols and phthalates in relation to

- child social behavior: applying an evidence-based prioritization to a cohort with improved exposure assessment. *Environ Health Perspect* 131(8):087006, PMID: 37556305, <https://doi.org/10.1289/EHP11798>.
- Zhou J, Chen XH, Zhang DD, Jin MC, Zhuang L, Du Y. 2022. Determination of multiple bisphenol analogues and their metabolites in human serum by liquid chromatography tandem mass spectrometry. *Environ Pollut* 312:120092, PMID: 36064063, <https://doi.org/10.1016/j.envpol.2022.120092>.
- Giulivo M, Lopez de Alda M, Capri E, Barcelo D. 2016. Human exposure to endocrine disrupting compounds: their role in reproductive systems, metabolic syndrome and breast cancer. A review. *Environ Res* 151:251–264, PMID: 27504873, <https://doi.org/10.1016/j.envres.2016.07.011>.
- Rancière F, Lyons JG, Loh VHY, Botton J, Galloway T, Wang T, et al. 2015. Bisphenol A and the risk of cardiometabolic disorders: a systematic review with meta-analysis of the epidemiological evidence. *Environ Health* 14:46, PMID: 26026606, <https://doi.org/10.1186/s12940-015-0036-5>.
- Ahn Y-A, Baek H, Choi M, Park J, Son SJ, Seo HJ, et al. 2020. Adipogenic effects of prenatal exposure to bisphenol S (BPS) in adult F1 male mice. *Sci Total Environ* 728:138759, PMID: 32403013, <https://doi.org/10.1016/j.scitotenv.2020.138759>.
- Asimakopoulos AG, Xue J, De Carvalho BP, Iyer A, Abualnaja KO, Yaghtmoor SS, et al. 2016. Urinary biomarkers of exposure to 57 xenobiotics and its association with oxidative stress in a population in Jeddah, Saudi Arabia. *Environ Res* 150:573–581, PMID: 26654562, <https://doi.org/10.1016/j.envres.2015.11.029>.
- Zeng J, Li J, Liu S, Yang Z, Zhong Y, Chen X, et al. 2021. Lipidome disturbances in preadipocyte differentiation associated with bisphenol A and replacement bisphenol S exposure. *Sci Total Environ* 753:141949, PMID: 32891999, <https://doi.org/10.1016/j.scitotenv.2020.141949>.
- Trefts E, Gannon M, Wasserman DH. 2017. The liver. *Curr Biol* 27(21):R1147–R1151, PMID: 29112863, <https://doi.org/10.1016/j.cub.2017.09.019>.
- Qin Y, Grimm SA, Roberts JD, Chrysovergis K, Wade PA. 2020. Alterations in promoter interaction landscape and transcriptional network underlying metabolic adaptation to diet. *Nat Commun* 11(1):962, PMID: 32075973, <https://doi.org/10.1038/s41467-020-14796-x>.
- Craig AJ, Silveira MAD, Ma L, Revsine M, Wang L, Heinrich S, et al. 2023. Genome-wide profiling of transcription factor activity in primary liver cancer using single-cell ATAC sequencing. *Cell Rep* 42(11):113446, PMID: 37980571, <https://doi.org/10.1016/j.celrep.2023.113446>.
- Wilson GK, Tennant DA, McKeating JA. 2014. Hypoxia inducible factors in liver disease and hepatocellular carcinoma: current understanding and future directions. *J Hepatol* 61(6):1397–1406, PMID: 25157983, <https://doi.org/10.1016/j.jhep.2014.08.025>.
- D'Artista L, Moschopoulou AA, Barozzi I, Craig AJ, Seehawer M, Herrmann L, et al. 2023. MYC determines lineage commitment in KRAS-driven primary liver cancer development. *J Hepatol* 79(1):141–149, PMID: 36906109, <https://doi.org/10.1016/j.jhep.2023.02.039>.
- Bravo González-Blas C, Matetovic I, Hillen H, Taskiran II, Vandepoel R, Christiaens V, et al. 2024. Single-cell spatial multi-omics and deep learning dissect enhancer-driven gene regulatory networks in liver zonation. *Nat Cell Biol* 26(1):153–167, PMID: 38182825, <https://doi.org/10.1038/s41556-023-01316-4>.
- Li Z, Ren Y, Li X, Wang W. 2023. KDM2A interacts with estrogen receptor alpha to promote bisphenol A and S-induced breast cancer cell proliferation by repressing TET2 expression. *Ecotoxicol Environ Saf* 262:115132, PMID: 37315367, <https://doi.org/10.1016/j.ecoenv.2023.115132>.
- Sahoo PK, Pradhan LK, Das SK. 2022. Chronic bisphenol A exposure induces temporal neurobehavioral transformation and augmented chromatin condensation in the periventricular gray zone of zebrafish brain. *Drug Chem Toxicol* 45(6):2794–2803, PMID: 34670469, <https://doi.org/10.1080/01480545.2021.1991774>.
- Jung YH, Wang H-LV, Ruiz D, Bixler BJ, Linsenbaum H, Xiang J-F, et al. 2022. Recruitment of CTCF to an Fto enhancer is responsible for transgenerational inheritance of BPA-induced obesity. *Proc Natl Acad Sci USA* 119(50):e2214988119, PMID: 36469784, <https://doi.org/10.1073/pnas.2214988119>.
- Leung CT, Yang Y, Chan TF, Lin X, Wong AST, Lui WY, et al. 2023. Chromatin modifiers: a new class of pollutants with potential epigenetic effects revealed by in vitro assays and transcriptomic analyses. *Toxicology* 484:153413, PMID: 36581016, <https://doi.org/10.1016/j.tox.2022.153413>.
- EPA (US Environmental Protection Agency). 2015. *Bisphenol A Alternatives in Thermal Paper*. [https://www.epa.gov/sites/production/files/2015-08/documents/bpa\\_final.pdf](https://www.epa.gov/sites/production/files/2015-08/documents/bpa_final.pdf) [accessed 12 May 2025].
- EFSA Panel on Food Contact Materials, Enzyme and Processing Aids, Lambré C, Barat Baviera JM, Bolognesi C, Cocconcelli PS, et al. 2021. Scientific guidance for the submission of dossiers on food enzymes. *EFSA J* 19(10):e06851, PMID: 34721697.
- Li A, Zhuang T, Shi W, Liang Y, Liao C, Song M, et al. 2020. Serum concentration of bisphenol analogues in pregnant women in China. *Sci Total Environ* 707:136100, PMID: 31863985, <https://doi.org/10.1016/j.scitotenv.2019.136100>.
- Zhang W, Gao Y, Chen C, Li A, Ma X, Liang Y, et al. 2021. Bisphenol S promotes the formation of visceral fat in mice. *Environ Sci Technol Lett* 8(8):699–704, <https://doi.org/10.1021/acs.estlett.1c00419>.

32. Li WC, Ralphs KL, Tosh D. 2010. Isolation and culture of adult mouse hepatocytes. *Methods Mol Biol* 633:185–196, PMID: [20204628](#), [https://doi.org/10.1007/978-1-59745-019-5\\_13](https://doi.org/10.1007/978-1-59745-019-5_13).
33. Liu Q, Shao W, Weng Z, Zhang X, Ding G, Xu C, et al. 2020. In vitro evaluation of the hepatic lipid accumulation of bisphenol analogs: a high-content screening assay. *Toxicol In Vitro* 68:104959, PMID: [32763284](#), <https://doi.org/10.1016/j.tiv.2020.104959>.
34. Illumina. 2025. TruSeq Stranded mRNA Reference Guide. <https://support.illumina.com/downloads/truseq-stranded-mrna-reference-guide-100000040498.html> [accessed 12 May 2025].
35. Petroff RL, Williams C, Li J-L, MacDonald JW, Bammler TK, Richards T, et al. 2022. Prolonged, low-level exposure to the marine toxin, domoic acid, and measures of neurotoxicity in nonhuman primates. *Environ Health Perspect* 130(9):097003, PMID: [36102641](#), <https://doi.org/10.1289/EHP10923>.
36. Chen S, Zhou Y, Chen Y, Gu J. 2018. Fastp: an ultra-fast all-in-one FASTQ preprocessor. *Bioinformatics* 34(17):i884–i890, PMID: [30423086](#), <https://doi.org/10.1093/bioinformatics/bty560>.
37. Dobin A, Davis CA, Schlesinger F, Drenkow J, Zaleski C, Jha S, et al. 2013. STAR: ultrafast universal RNA-seq aligner. *Bioinformatics* 29(1):15–21, PMID: [23104886](#), <https://doi.org/10.1093/bioinformatics/bts635>.
38. Liao Y, Smyth GK, Shi W. 2014. featureCounts: an efficient general purpose program for assigning sequence reads to genomic features. *Bioinformatics* 30(7):923–930, PMID: [24227677](#), <https://doi.org/10.1093/bioinformatics/btt656>.
39. Love MI, Huber W, Anders S. 2014. Moderated estimation of fold change and dispersion for RNA-seq data with DESeq2. *Genome Biol* 15(12):550, PMID: [25516281](#), <https://doi.org/10.1186/s13059-014-0550-8>.
40. Yu G, Wang LG, Han Y, He QY. 2012. clusterProfiler: an R package for comparing biological themes among gene clusters. *OMICS* 16(5):284–287, PMID: [22455463](#), <https://doi.org/10.1089/omi.2011.0118>.
41. Corces MR, Trevino AE, Hamilton EG, Greenside PG, Sinnott-Armstrong NA, Vesuna S, et al. 2017. An improved ATAC-seq protocol reduces background and enables interrogation of frozen tissues. *Nat Methods* 14(10):959–962, PMID: [28846090](#), <https://doi.org/10.1038/nmeth.4396>.
42. Langmead B, Salzberg SL. 2012. Fast gapped-read alignment with bowtie 2. *Nat Methods* 9(4):357–359, PMID: [22388286](#), <https://doi.org/10.1038/nmeth.1923>.
43. Heinz S, Benner C, Spann N, Bertolino E, Lin YC, Laslo P, et al. 2010. Simple combinations of lineage-determining transcription factors prime cis-regulatory elements required for macrophage and B cell identities. *Mol Cell* 38(4):576–589, PMID: [20513432](#), <https://doi.org/10.1016/j.molcel.2010.05.004>.
44. Yu G, Wang LG, He QY. 2015. ChIPseeker: an R/bioconductor package for ChIP peak annotation, comparison and visualization. *Bioinformatics* 31(14):2382–2383, PMID: [25765347](#), <https://doi.org/10.1093/bioinformatics/btv145>.
45. Ramirez F, Dunder F, Diehl S, Gruning BA, Manke T. 2014. deepTools: a flexible platform for exploring deep-sequencing data. *Nucleic Acids Res* 42:W187–W191, PMID: [24799436](#), <https://doi.org/10.1093/nar/gku365>.
46. Targher G, Tilg H, Byrne CD. 2021. Non-alcoholic fatty liver disease: a multisystem disease requiring a multidisciplinary and holistic approach. *Lancet Gastroenterol Hepatol* 6(7):578–588, PMID: [33961787](#), [https://doi.org/10.1016/S2468-1253\(21\)00020-0](https://doi.org/10.1016/S2468-1253(21)00020-0).
47. Martinez MA, Blanco J, Rovira J, Kumar V, Domingo JL, Schuhmacher M. 2020. Bisphenol A analogues (BPS and BPF) present a greater obesogenic capacity in 3T3-L1 cell line. *Food Chem Toxicol* 140:111298, PMID: [32220626](#), <https://doi.org/10.1016/j.fct.2020.111298>.
48. Ahmed S, Atlas E. 2016. Bisphenol S- and bisphenol A-induced adipogenesis of murine preadipocytes occurs through direct peroxisome proliferator-activated receptor gamma activation. *Int J Obes (Lond)* 40(10):1566–1573, PMID: [27273607](#), <https://doi.org/10.1038/ijo.2016.95>.
49. Meng Z, Wang D, Liu W, Li R, Yan S, Jia M, et al. 2019. Perinatal exposure to bisphenol S (BPS) promotes obesity development by interfering with lipid and glucose metabolism in male mouse offspring. *Environ Res* 173:189–198, PMID: [30921577](#), <https://doi.org/10.1016/j.envres.2019.03.038>.
50. Qin J, Ru S, Wang W, Hao L, Ru Y, Wang J, et al. 2020. Long-term bisphenol S exposure aggravates non-alcoholic fatty liver by regulating lipid metabolism and inducing endoplasmic reticulum stress response with activation of unfolded protein response in male zebrafish. *Environ Pollut* 263(pt B):114535, PMID: [32283406](#), <https://doi.org/10.1016/j.envpol.2020.114535>.
51. Chen BP, Liang G, Whelan J, Hai T. 1994. ATF3 and ATF3 Delta zip. Transcriptional repression versus activation by alternatively spliced isoforms. *J Biol Chem* 269(22):15819–15826, PMID: [7515060](#), [https://doi.org/10.1016/S0021-9258\(17\)40754-X](https://doi.org/10.1016/S0021-9258(17)40754-X).
52. Ku HC, Cheng CF. 2020. Master regulator activating transcription factor 3 (ATF3) in metabolic homeostasis and cancer. *Front Endocrinol (Lausanne)* 11:556, PMID: [32922364](#), <https://doi.org/10.3389/fendo.2020.00556>.
53. Allen-Jennings AE, Hartman MG, Kociba GJ, Hai T. 2001. The roles of ATF3 in glucose homeostasis. A transgenic mouse model with liver dysfunction and defects in endocrine pancreas. *J Biol Chem* 276(31):29507–29514, PMID: [11371557](#), <https://doi.org/10.1074/jbc.M100986200>.
54. Pramfalk C, Ahmed O, Pedrelli M, Minniti ME, Luquet S, Denis RG, et al. 2022. Soat2 ties cholesterol metabolism to beta-oxidation and glucose tolerance in male mice. *J Intern Med* 292(2):296–307, PMID: [34982494](#), <https://doi.org/10.1111/joim.13450>.
55. Buhman KK, Accad M, Novak S, Choi RS, Wong JS, Hamilton RL, et al. 2000. Resistance to diet-induced hypercholesterolemia and gallstone formation in ACAT2-deficient mice. *Nat Med* 6(12):1341–1347, PMID: [11100118](#), <https://doi.org/10.1038/82153>.
56. Yu C, Li Y, Li S, Zeng F, Yu J, et al. 2024. A novel mechanism for regulating lung immune homeostasis: Zukamu granules alleviated acute lung injury in mice by inhibiting NLRP3 inflammasome activation and regulating Th17/treg cytokine balance. *J Ethnopharmacol* 324:117831, PMID: [38280662](#), <https://doi.org/10.1016/j.jep.2024.117831>.
57. Aldridge DL, Moodley D, Park J, Phan AT, Rausch M, White KF, et al. 2024. Endogenous IL-27 during toxoplasmosis limits early monocyte responses and their inflammatory activation by pathological T cells. *mBio* 15(3):e0008324, PMID: [38376210](#), <https://doi.org/10.1128/mbio.00083-24>.
58. Liu S, Li Z, Lan S, Hao H, Baz AA, Yan X, et al. 2024. The dual roles of activating transcription factor 3 (ATF3) in inflammation, apoptosis, ferroptosis, and pathogen infection responses. *Int J Mol Sci* 25(2):824, PMID: [38255898](#), <https://doi.org/10.3390/ijms25020824>.
59. Bejjani F, Evanno E, Zibara K, Piechaczyk M, Jariel-Encontre I. 2019. The AP-1 transcriptional complex: local switch or remote command? *Biochim Biophys Acta Rev Cancer* 1872(1):11–23, PMID: [31034924](#), <https://doi.org/10.1016/j.bbcan.2019.04.003>.
60. Xu Y, Hu S, Jadhav K, Zhu Y, Pan X, Bawa FC, et al. 2021. Hepatocytic activating transcription factor 3 protects against steatohepatitis via hepatocyte nuclear factor 4alpha. *Diabetes* 70(11):2506–2517, PMID: [34475098](#), <https://doi.org/10.2337/db21-0181>.